Journal of Solid State Electrochemistry (2022) 26:1941–1950
https://doi.org/10.1007/s10008-022-05142-w

ORIGINAL PAPER

Aqueous spray-drying synthesis of alluaudite $Na_{2+2x}Fe_{2-x}(SO_4)_3$ sodium insertion material: studies of electrochemical activity, thermodynamic stability, and humidity-induced phase transition

Pubali Barman[1] · Debasmita Dwibedi[1,2] · K. Jayanthi[3] · Sher Singh Meena[4] · Supreeth Nagendran[5,6] · Alexandra Navrotsky[3] · Prabeer Barpanda[1,7]

Received: 8 February 2022 / Revised: 16 February 2022 / Accepted: 21 February 2022 / Published online: 4 March 2022

Abstract

In pursuit of high-energy density sodium insertion materials, polyanionic frameworks can be designed with tuneable high-voltage operation stemming from inductive effect. *Alluaudite* $Na_2Fe_2(SO_4)_3$ polysulfate forms one such earth-abundant compound registering the highest Fe^{3+}/Fe^{2+} redox potential (ca. 3.8 V vs. Na/Na^+). While this SO_4-based system exhibits high voltage operation, it is prone to thermal decomposition and moisture attack leading to hydrated derivatives, making its synthesis cumbersome. Also, the Na–Fe–S–O quaternary system is rich with (anhydrous to hydrated) phase transitions. Herein, we demonstrate scalable aqueous-based spray drying synthesis of *alluaudite* $Na_{2+2x}Fe_{2-x}(SO_4)_3$ sodium insertion material involving the formation of *bloedite* $Na_2Fe(SO_4)_2{\cdot}4H_2O$ as an intermediate phase. Moreover, a reversible phase transition from alluaudite to bloedite under controlled conditions of temperature and relative humidity is reported for the first time. Thermochemistry measurements revealed the enthalpies of formation (ΔH°_f) of *alluaudite* and *bloedite* are exothermic. Hydrated *bloedite* ($\Delta H^\circ_f = -117.16 \pm 1.10$ kJ/mol) was found to be significantly more energetically stable than anhydrous alluaudite ($\Delta H^\circ_f = -11.76 \pm 1.25$ kJ/mol). The calorimetric data support the observed synthesis and transformation (hydration-dehydration) pathways. Spray drying route led to spherical morphology delivering capacity ~80 mAh/g. Spray drying can be extended for rapid economic synthesis of sulfate class of battery materials.

Keywords Sodium-ion battery · Cathode · Alluaudite · Capacity · Phase transition

Pubali Barman and Debasmita Dwibedi contributed equally to this work.

✉ Prabeer Barpanda
prabeer@iisc.ac.in

1 Faraday Materials Laboratory (FaMaL), Materials Research Center, Indian Institute of Science, Bangalore 560012, India

2 Department of Chemical System Engineering, The University of Tokyo, 7-3-1 Hongo, Bunkyo-ku, Tokyo 113-8656, Japan

3 School of Molecular Sciences and Navrotsky Eyring Center for Materials of the Universe, Arizona State University, Tempe, AZ 85287, USA

4 Solid State Physics Division, Bhabha Atomic Research Centre, Mumbai 400085, India

5 Department of Chemistry, Central College, Bangalore University, Bangalore 560001, India

6 Department of Chemistry, University of Cambridge, Lensfield Road, Cambridge CB2 1EW, UK

7 Helmholtz Institut Ulm (HIU), Helmholtzstrasse 11, Ulm 89081, Germany

Introduction

Rechargeable batteries rule the energy storage sector in the twenty-first century. Batteries broadly cater to two kinds of applications: volume/weight-restricted application like electronic gadgets/electric automobiles and volume/weight-independent usages like stationary grid storage. While lithium-ion batteries (LIBs) are irreplaceable for the former category, the latter can be propelled by economic sodium-ion batteries (SIBs) [1]. To realize practical SIBs with high energy density, suites of oxides and polyanionic insertion materials have been unveiled. While oxides can deliver high capacity, polyanionic compounds are particularly known for their high-voltage operation, thermal/chemical stability, and operational safety. Particularly exploiting the inductive effect, simply by changing the electronegative polyanionic moieties (S > W > P > Mo), the working potential of the cathode material can be tuned [2, 3]. On another note, material economy can be realized by combining earth-abundant alkali

(e.g., Na) and transition metal (e.g., Fe) chemistry. Some such examples are $NaFeO_2$, $Na_x[Fe_{1/2}Mn_{1/2}]O_2$, $NaFePO_4$, Na_2FePO_4F, $Na_2FeP_2O_7$, and $Na_4Fe_3(PO_4)_2(P_2O_7)$, each operating around 3 V [1, 4]. To enhance the overall nominal voltage of polyanionic compounds, the phosphate group can be substituted by highly electronegative sulfate group (SO_4^{2-}) [2, 5]. Using this strategy, in 2014, Yamada group reported sulfate-based alluaudite class of high-voltage cathode material [6].

Alluaudites, named after its discoverer François Alluaud II, are a group of alkali metal phosphate–based naturally occurring minerals having open frameworks as well as broad tunnels for easy alkali ion passage [7]. The general formula of alluaudite-based materials can be written as $A(1)A(2)M(1)M(2)_2(XO_4)_3$, where A denotes the alkali ions, M denotes the transition metal ions, and X could be S, P, As, V, Mo, or W [8]. A and $M(1)$ sites are occupied by monovalent (Na^+, Li^+) or divalent cations (Ca^{2+}, Mg^{2+}) while the $M(2)$ site can be filled with divalent (Mn^{2+}, Fe^{2+}) or trivalent cations (Mn^{3+}, Fe^{3+}, In^{3+}). The MO_6 octahedra and XO_4 tetrahedra are connected to form two tunnels along the c direction within the structure. $A(1)$ and $A(2)$ sites, occupied by alkali ions, are situated inside these tunnels capable of ion mobility within the alluaudite framework. Delmas group reported the first alluaudite type cathode $NaMnFe_2(PO_4)_3$ for SIBs albeit with poor activity as well as low working voltage [9]. To overcome the voltage issue, Yamada group reported the first SO_4^{2-}-based alluaudite material $Na_2Fe_2(SO_4)_3$ registering the highest Fe^{3+}/Fe^{2+} redox potential (ca. 3.8 V vs. Na/Na^+). This discovery ushered further research on $Na_{2+2x}M_{2-x}(SO_4)_3$ alluaudite class of SIB cathode materials [10–15]. While these sulfate-based alluaudites offer high working voltage and energy density, their syntheses remain cumbersome. While the solid-state route warrants prolonged mechanical milling and annealing duration, ionothermal route can be expensive. Most synthesis routes cannot directly use commercially available $FeSO_4{\cdot}7H_2O$ precursor, but instead use its anhydrous derivatives $FeSO_4{\cdot}nH_2O$ ($n = 0.1$).

In the present work, we report spray-drying synthesis (SDS) as a solvothermal method for scalable synthesis of alluaudite $Na_{2+2x}Fe_{2-x}(SO_4)_3$ insertion material directly using commercial $FeSO_4{\cdot}7H_2O$ precursor. This two-step route involves the formation of bloedite $Na_2Fe(SO_4)_2{\cdot}4H_2O$ as an intermediate phase followed by its transition to the alluaudite target material. SDS facilitates the formation of spherical morphology along with restricted annealing duration. We further report the use of X-ray diffraction under controlled condition of relative humidity (RH-XRD) for gauging potential moisture attack on alluaudite. Upon varying humidity from 10 to 90%, a systematic alluaudite-to-bloedite phase transition was observed, while opposite phase transition (i.e., bloedite-to-alluaudite) was noticed upon annealing. The thermodynamics of formation and dehydration, measured by calorimetric techniques, confirms the stability of the hydrated bloedite phase and the observed transformation at high temperature. The SDS prepared alluaudite can deliver 77% of the theoretical capacity retaining high redox potential without any cathode optimization or conductive additives.

Materials and methods

Synthesis The target alluaudite was prepared by solution-based spray-drying synthesis (SDS) method using a Büchi B-90 spray dryer connected to a peristaltic pump. A uniform aqueous slurry was prepared containing a stoichiometric mixture of commercial precursors Na_2SO_4 (SDFCL, 99.5%) and $FeSO_4{\cdot}7H_2O$ (SDFCL, 99.5%). Unlike the classical solid-state route, the incorporation of aqueous medium assured atomic-level mixing and labile ionic diffusion [16]. Spray drying is a method of producing dry powders from precursor solution by atomization in small droplets (spray) and evaporation (drying) at the droplet surface at increased temperature. Here, the precursor slurry was passed through the nozzle of the spray dryer, leading to nebulization and rapid transformation into solids upon exposure of tiny droplets with hot air. For spray drying, the inlet and outlet temperatures were maintained at 200 °C and 80 °C respectively. The spray-dried powder was collected using cyclone separators, bag filters, electrostatic precipitator, and wet scrubbers. This intermediate dried complex was pelletized and annealed at 350 °C for 6–8 h in a tubular furnace maintained under steady argon flow. Ascorbic acid ($C_6H_8O_6$, Sigma, 99%) can be optionally added in the initial slurry to facilitate the formation of in situ carbon coating on the target material. The SDS route can yield desired materials either at low annealing temperature and/or shorter annealing duration, which in turn yields particles with minimal grain growth, facilitating superior electrochemical activity.

Structural and physical characterization The powder X-ray diffraction (PXRD) patterns were acquired with a PANalytical Empyrean X-ray diffractometer equipped with a Cu $K\alpha$ source ($\lambda_1 = 1.5405$ Å, $\lambda_2 = 1.5443$ Å) operating at 40 kV/30 mA. Rietveld analysis was performed using GSAS-I program with EXPGUI graphical interface [17–19]. The background, scale factor, lattice parameter, profile functions, and phase parameters were refined. Crystal structures were illustrated using the VESTA-3 software [20]. To probe the material stability upon moisture exposure, in situ XRD patterns were collected with a Bruker D8 Advance X-ray diffractometer (Cu $K\alpha$ source, $\lambda_1 = 1.5405$ Å, $\lambda_2 = 1.5443$ Å, operating at 40 kV/30 mA) equipped with an Anton Paar CHC plus$^+$ humidity chamber attachment with water inlet/outlet. XRD patterns were collected after exposing the

sample to various degrees of humidity (RH = 10% to 90%). Thermal analysis (TGA–DSC) of ~20 mg of the intermediate compound was conducted with a Mettler Toledo instrument in the temperature range of 25–400 °C (under steady nitrogen flow) with a heating rate of 5 °C/min. Fourier transform infrared (FTIR) spectrum was collected with a PerkinElmer instrument in attenuated total reflectance (ATR) mode within the spectral range of 4000–650 cm^{-1}. Raman spectra were recorded with a Horiba Jobin Yvon HR-Raman-123 MicroPL spectrometer with a green laser source (λ = 519 nm) to check the presence of carbon coating.

Particle morphology was inspected by a Carl Zeiss Ultra55 field emission scanning electron microscope (FESEM, tungsten source) operating at 0.1–30 kV. Gold sputtering was conducted on the powder sample, sprinkled over a double-sided carbon tape, for 120 s. Selected area electron diffraction (SAED) pattern and the high-resolution transmission electron microscopy (HRTEM) images were obtained by a Titan Themis (Thermo-FEI, at 300 kV) transmission electron microscope. For the TEM study, the powder sample was dispersed in absolute ethanol and was drop-casted on a holey carbon-copper grid. Elemental distribution was detected using an EDS analyzer equipped with the aforementioned TEM instrument.

Mössbauer measurements Ambient temperature Mössbauer spectra (MS) were recorded with a conventional spectrometer with ^{57}Co source in Rh matrix of 3 mCi operating in constant acceleration mode in transmission geometry. They were analyzed using the WinNormos site fit program. The calibration of the velocity scale was done by using an enriched α-^{57}Fe metal foil. The isomer shift values are relative to Fe metal foil ($\delta = 0.0$ mm/s). Mössbauer spectra of both the spray-dried intermediate and the desired alluaudite phase were fitted with four symmetric doublets.

Thermochemistry study PXRD and TG-DSC measurements were performed before and after the calorimetric measurement to detect any possible decomposition and to check for adsorbed water on the sample due to exposure in the ambient atmosphere prior to solution calorimetric experiments. Dissolution enthalpy of $Na_{2.27}Fe_{1.86}(SO_4)_3$ in 5 N HCl was measured using both CSC 4400 isothermal (with IMC data acquisition software) and Hart Scientific (with Labview software) microcalorimeters with mechanical stirring of the samples and reagents at 25 °C. The calorimeters were calibrated with KCl (NIST standard reference material) by dissolving 15 mg pellets in 25 g of water at 25 °C. The solution enthalpy of this reference concentration (0.008 mol kg^{-1}), deduced from the literature and the enthalpy of dilution measurements [21], was used to obtain the calorimeter calibration factor.

In a typical calorimetric run, 6 – 8 mg of the sample was pressed into a pellet and then dropped into 25 g of 5 N HCl placed in the sample chamber of the calorimeter. The sample dissolution causes heat flow due to temperature difference and is recorded as a microvolt calorimetric signal. The integrated area under the recorded microwatt signal relative to a linear baseline corresponds to the total heat effect which on conversion into joules with KCl calibration corresponds to the enthalpy of sample dissolution (ΔH_{ds}). An appropriate thermochemical cycle based on Hess' law (difference in the heat of solution of products and reactants) was used to calculate the enthalpy of formation. This methodology is essentially the same as that used in prior studies [22].

Electrochemical characterization For electrode performance analysis, the working electrode was prepared from an intimate slurry containing 70 wt% of active material, 20 wt% of carbon black (Super-P) (Alfa Aesar), and 10 wt% polyvinylidene fluoride (PVDF) (Sigma Aldrich) binder in a minimal amount of *N*-methyl-2-pyrrolidone (NMP) (Sigma Aldrich) solvent. This slurry was uniformly coated on an Al foil acting as current collector followed by a vacuum drying at 120 °C for 12 h to remove the NMP. Circular disks (acting as working electrode) were punched with active material loading ~ 3–5 mg/cm^2. CR2032 type coin cells were assembled inside an Ar-filled glove box (MBraun LabStar GmbH, O_2 and $H_2O < 0.5$ ppm) to avoid any moisture contamination. The working electrode and sodium metal foil (as counter electrode) were separated by a sheet of Whatman GF/C glass fiber separator soaked with 1 M $NaPF_6$ in ethylene carbonate/diethyl carbonate (EC:DEC; 1:1 vol) electrolyte (battery grade, Kishida Chemicals). The electrochemical testing was performed (at 25 °C) using the Neware BTS-4000 battery tester in the potential window of 2–4.5 V at a rate of C/20 (1C = 100 mAh/g).

Result and discussions

While the alluaudite $Na_{2+2x}Fe_{2-x}(SO_4)_3$ offers high energy density–powered by its 3.8 V activity along with fast kinetics, the presence of SO_4 moieties makes it moisture sensitive and prone to thermal decomposition at temperature > 450 °C. The sulfate compounds can be air-sensitive resulting in a poor electrochemical performance and structural stability. Thus, classical solid-state and aqueous solvothermal routes are ruled out. On another note, the Na–Fe–S–O quaternary system is rich with several intermediate phases and their hydrated derivatives like *krohnkite* [$Na_2Fe(SO_4)_2{\cdot}2H_2O$], *bloedite* [$Na_2Fe(SO_4)_2{\cdot}4H_2O$], and *vanthoffite* [$Na_6Fe(SO_4)_4$], which are thermodynamically more stable than (off) stoichiometric alluaudites [$Na_{2+2x}Fe_{2-x}(SO_4)_3$]. Therefore, apart from the solid-state (dry) route, alluaudite has been prepared by non-aqueous

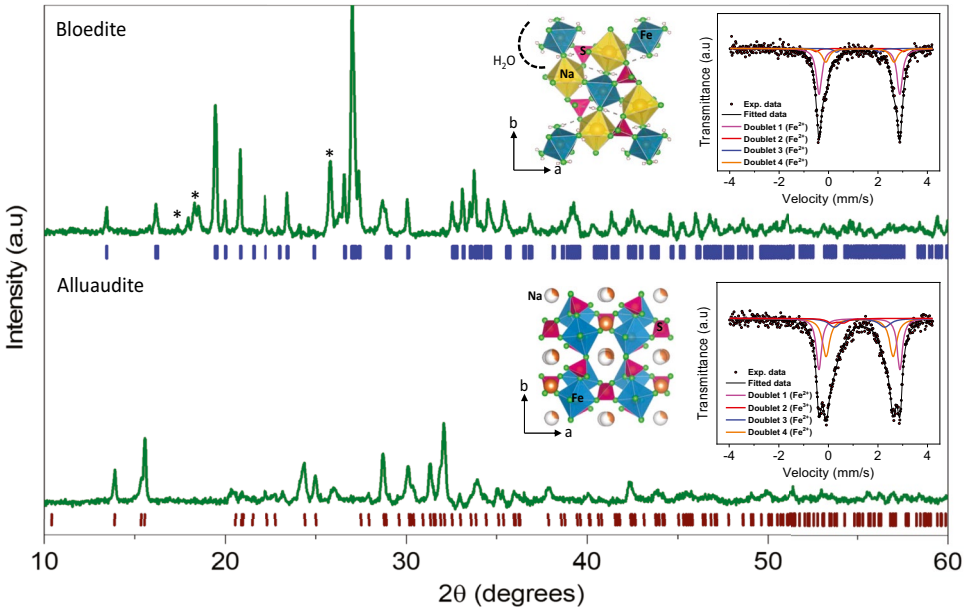

Fig. 1 Comparative X-ray diffraction patterns and corresponding Mössbauer spectra of (top) spray drying–induced intermediate product (bloedite) and (bottom) final alluaudite $Na_{2.27}Fe_{1.86}(SO_4)_3$ material after annealing at 350 °C for 6–8 h. The intermediate product was found to be majorly bloedite $Na_2Fe(SO_4)_2{\cdot}4H_2O$ with few unidentified peaks marked by asterisk marks. The corresponding structures are shown in the insets. In both cases, Mössbauer spectra confirm the presence of mostly Fe^{2+} species

solvothermal (e.g., hydrophobic ionic liquid) route [14] and indirect (dehydration) synthesis using bloedite [23]. In addition, the complexity in alluaudite synthesis arises from the Fe precursor $FeSO_4{\cdot}7H_2O$ (*melanterite*), which can convert to various anhydrous derivatives such as $FeSO_4{\cdot}6H_2O$ (*ferrohexahydrite*), $FeSO_4{\cdot}5H_2O$ (*siderotil*), $FeSO_4{\cdot}4H_2O$ (*rozenite*), $FeSO_4{\cdot}H_2O$ (*szomolnokite*), and anhydrous $FeSO_4$ upon annealing. Further, it can convert to various hydrated derivatives like $Fe_5(SO_4)_6(OH)_2{\cdot}20H_2O$ (*copiapite*) and $Fe_2(SO_4)_3{\cdot}11H_2O$ (*quenstedtite*) etc. [24]. All these derivatives offer varied reaction kinetics for alluaudite formation making its synthesis tricky. Here, two-step spray drying synthesis [15] was implemented for preparation of target alluaudite having twin benefits of using aqueous (wet chemistry) reacting media and direct use of widely available $FeSO_4{\cdot}7H_2O$ precursor.

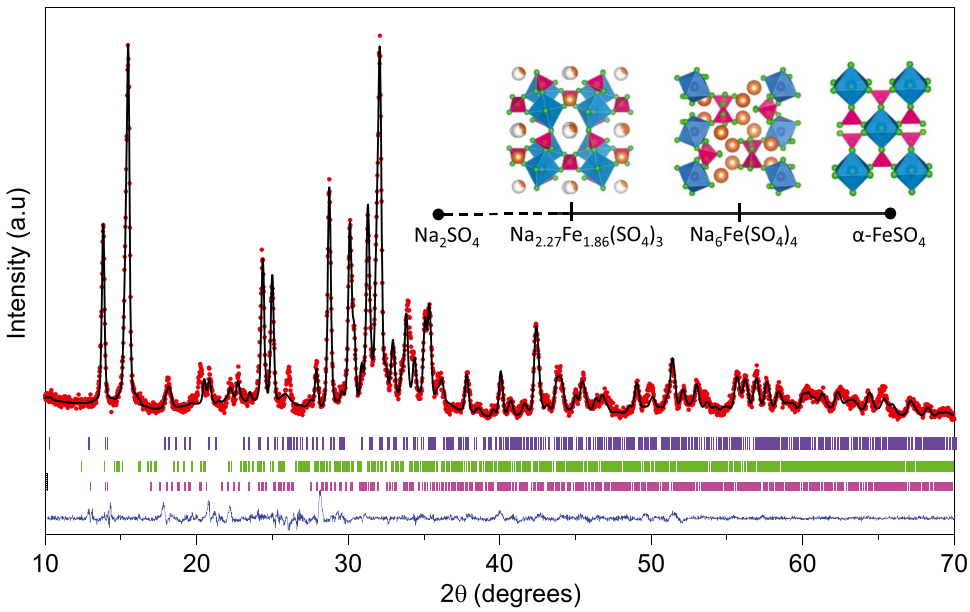

Fig. 2 Rietveld refined XRD powder diffraction pattern of spray drying prepared alluaudite material. The experimental data points (red dots), calculated patterns (black line), their difference (blue line), and the Bragg peaks [violet ticks for $Na_{2.27}Fe_{1.86}(SO_4)_3$, green ticks for α-$FeSO_4$ and pink ticks for $Na_6Fe(SO_4)_4$] are shown. Small amount of thermodynamically stable α-$FeSO_4$ and vanthoffite $Na_6Fe(SO_4)_4$ impurities were noticed, which are structurally illustrated in the inset in the Na_2SO_4-$FeSO_4$ binary system

Table 1 Mössbauer parameters of intermediate complex $Na_2Fe(SO_4)_2{\cdot}4H_2O$ (NFS1) and final material $Na_{2+2x}Fe_{2-x}(SO_4)_3$ (NFS2)

Sample	Fe sites	Quadrupole splitting (ΔE_Q) mm/s ±0.008	Isomer shift (δ) mm/s ±0.002	Line width (Γ) mm/s ±0.005	Relative Area, R_A (%)	Goodness of fit (χ^2)
NFS1	Doublet 1 (Fe^{2+})	3.266	1.248	0.267	61.3	1.008
	Doublet 2 (Fe^{2+})	3.547	1.264	0.268	4.2	
	Doublet 3 (Fe^{2+})	1.722	1.186	0.250	4.5	
	Doublet 4 (Fe^{2+})	2.760	1.267	0.342	30.0	
NFS2	Doublet 1 (Fe^{2+})	3.267	1.252	0.256	28.5	0.983
	Doublet 2 (Fe^{3+})	0.478	0.368	0.445	7.0	
	Doublet 3 (Fe^{2+})	2.029	1.259	0.558	23.0	
	Doublet 4 (Fe^{2+})	2.708	1.260	0.357	41.5	

Spray drying–induced nebulized precursor solution, where each nebula can be thought of as a spherical "nano-reactor," quickly transformed to an intermediate complex upon exposure to hot air. This intermediate complex was found to consist of majorly bloedite $Na_2Fe(SO_4)_2{\cdot}4H_2O$ phase (Fig. 1). It comes as no surprise as bloedite is a stable complex in the Na_2SO_4–$FeSO_4$ binary system. Thermal analysis of this spray-dried intermediate complex revealed a series of endothermic peaks with no weight loss after 300 °C (Fig. S1, ESI). Taking a hint from the thermal analysis, the intermediate complex was annealed at 350 °C for 6-8 h (in Ar flow) involving dehydration to yield the desired alluaudite phase. Rietveld analysis of the final material confirmed that major diffraction peaks can be indexed to the alluaudite phase (97.01%) with minor stable secondary phases like α-$FeSO_4$ (1.98%) and *vanthoffite* $Na_6Fe(SO_4)_4$ (1.01%) (Fig. 2). Using the model structure proposed by Oyama et al. [13], the atomic positions, occupancy, and thermal parameters of Na, Fe, S, and O atoms were refined to fit the major peaks. Rietveld refinement confirmed the formation of an off-stoichiometric $Na_{2.27}Fe_{1.86}(SO_4)_3$ alluaudite material crystallizing in monoclinic structure (s.g. *C*2/*c*) (Table S1, ESI). Despite varying the thermal treatment conditions, alluaudite materials were found to have an inherent tendency to form off-stoichiometric compositions.

The environment of constituent iron in the intermediate and annealed final materials was further gauged by room temperature Mössbauer analysis (Fig. 1, inset). The corresponding refined Mössbauer parameters [quadrupole splitting (Δ), isomer shifts (δ), line width (Γ) and relative area (R_A)] are given in Table 1. Despite synthesis in aqueous media, no significant Fe oxidation was noticed with the

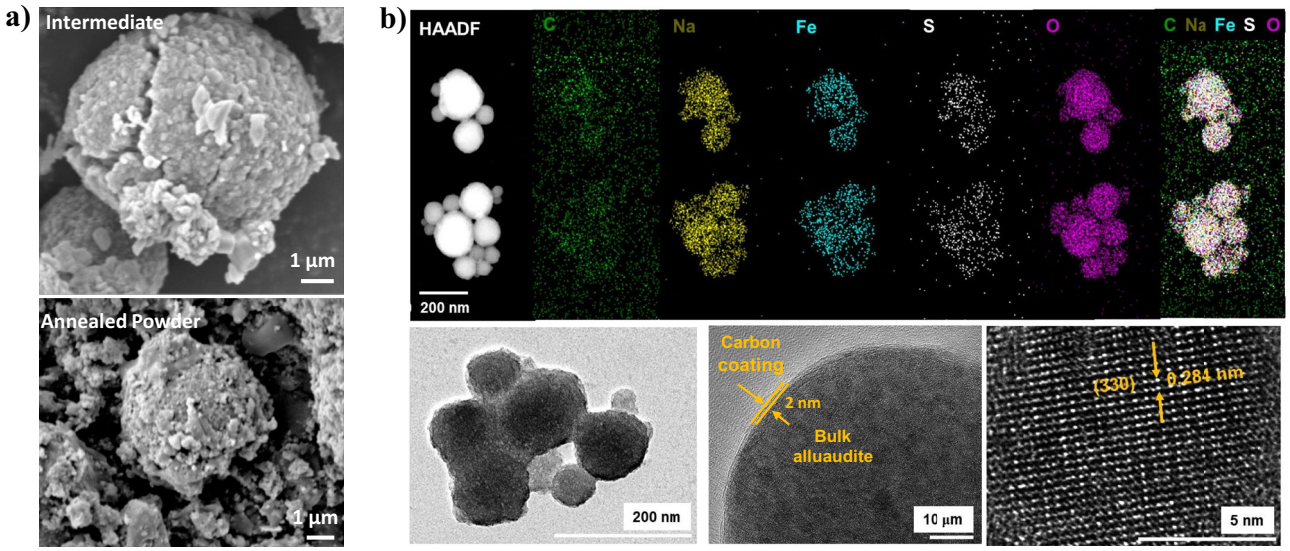

Fig. 3 Microstructural insights into the spray-dried synthesized $Na_{2.27}Fe_{1.86}(SO_4)_3$ alluaudite. **a** SEM micrographs depicting the spherical morphology both (top) intermediate phase and (bottom) alluaudite phase. **b** Representative annular dark field HAADF image and the corresponding elemental mapping revealing nanospheres having uniform distribution of all constituent elements (Na, Fe, S, O). A thin ~ 2-nm carbon coating on alluaudite material was captured in TEM micrograph. High-resolution TEM image revealed the atomic fringes with interplanar distance of 0.284 nm (for (330) plane) attesting the crystallinity of the compound

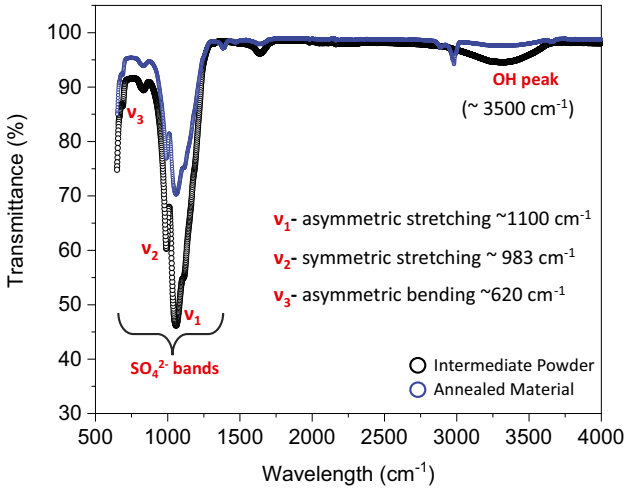

Fig. 4 Comparative FT-infrared spectra of spray drying intermediate product and final alluaudite showing different vibrational bands arising from constituent SO_4 tetrahedral building blocks. The intermediate product (hydrated bloedite) has a hump ~3400 cm^{-1}, which is absent in case of the annealed (dehydrated alluaudite) material

materials consisting majorly Fe^{2+} species with minimal Fe^{3+} impurities. As Fe^{2+}-based sulfate systems tend to oxidize, the addition of a pinch of ascorbic acid in precursor slurry can stabilize the Fe^{2+} environment in both the intermediate and final phase, as confirmed from Mössbauer analysis.

Following, the morphology of spray-dried materials was examined using electron microscopy tools. SDS is a colloidal/solution-assisted self-assembly process which leads to the rapid formation of droplets in presence of hot air. Thus, it leads to spherical morphology in the intermediate as well as the final material as observed with the SEM images (Fig. 3a). A closer look at the surface morphology further suggests the as-annealed powder possessed rough and protrusion spherical exteriors with agglomeration. The high-angle annular dark-field imaging (HAADF) and TEM micrographs (Fig. 3b) further attest to the spherical morphology of the as-synthesized alluaudite depicting the rich nanospheres interconnected with carbon networks. The carbon network/coating arises from the addition of a nominal amount of ascorbic acid in the precursor solution. High-resolution TEM pattern displayed good crystallinity with the indexed space group (*C*2/*c*). Energy-dispersive (EDS) elemental analysis confirmed homogeneous distribution of all selected elements: Na, Fe, S, O, and C. Further, an off-stoichiometric sodium-rich and iron-deficient environment was reaffirmed in sync with Rietveld (X-ray) analysis.

Unlike the oxides and other polyanionic moieties (PO_4^{3-}, MoO_4^{2-}, SiO_4^{4-}, etc.), the sulfates are intrinsically prone to moisture attack due to the Lewis basicity of oxygen atom in SO_4^{2-} commensurate with that of H_2O [25]. To gauge the effect of moisture on the as-prepared sample, FT-infrared

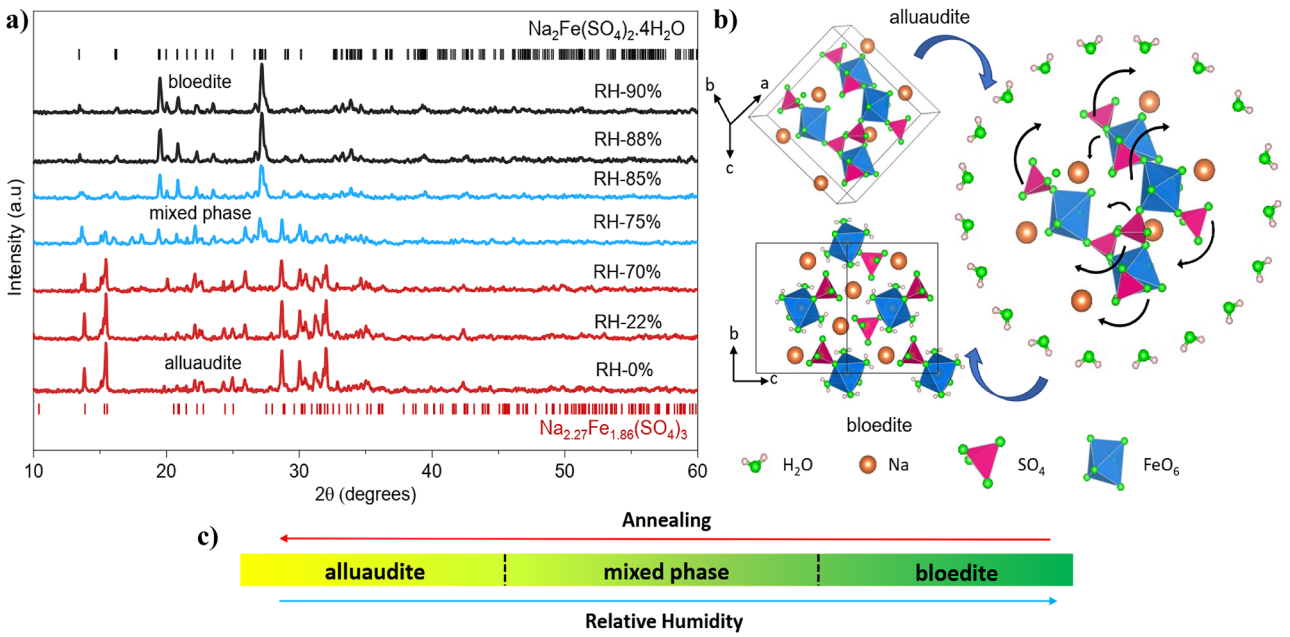

Fig. 5 **a** Variation in X-ray diffraction patterns of pristine alluaudite subjected to different degree of relative humidity (10 ~ 90% of RH). While alluaudite phase was retained until RH 70%, a mixture of phases was noticed above that, which completely converted to hydrated bloedite above RH 88%. **b** Schematic presentation depicting alluaudite to bloedite phase transformation under influence of humidity. Exposure to humidity leads to the presence of structural water molecules and reorientation of FeO_6 octahedral units to undergo alluaudite to bloedite phase transition. **c** Depiction of reversible phase transition from alluaudite to bloedite (upon hydration) and bloedite to alluaudite (upon annealing)

Table 2 Calorimetric data of alluaudite $Na_2Fe_2(SO_4)_3$ and bloedite $Na_2Fe(SO_4)_2{\cdot}4H_2O$

Composition	ΔH_{ds} (kJ/mol)	$\Delta H°_f$ (kJ/mol)
Na_2SO_4	20.65 ± 0.40 (6)	
$FeSO_4$	−35.44 ± 0.42 (5) [27]	
H_2O	−0.54 [28]	
$Na_2Fe_2(SO_4)_3$	−38.47 ± 0.84(7)	−11.76 ± 1.25
$Na_2Fe(SO_4)_2{\cdot}4H_2O$	100.21 ± 0.94(6)	−117.16 ± 1.10

Errors are two standard deviations of the mean. Values in parenthesis are the number of measurements

spectra of both spray dried powders and post annealed samples were examined (Fig. 4). The intermediate complex showed a broad band ~3500 cm^{-1} (related to symmetric/asymmetric stretching of OH^- species) revealing the presence of structural water in bloedite composition. However, the post-annealed phase was found to have no residual H_2O or surface-adsorbed moisture even though prepared via an aqueous route. Also, low wavenumber signature bands stemming from SO_4^{2-} species were observed. Three different kinds of infrared bands were captured: two from stretching vibration of SO_4 units [asymmetric stretching $\nu_1 \approx 1100$ cm^{-1} and symmetric stretching $\nu_2 \approx 983$ cm^{-1}] and one from bending vibration of SO_4 units [asymmetric bending $\nu_3 \approx 620$ cm^{-1}]. The incorporation of thin carbon coating arising from carbon sources (ascorbic acid) was further verified by Raman spectroscopy, where signature D (~1390 cm^{-1}) and G (~1595 cm^{-1}) bands were captured arising from elemental carbon (Fig. S2, ESI). A relatively sharper G band hinted at the graphitic nature of the carbon coating, which can be beneficial for overall cathode electrochemical performance.

While the sulfate-based electrode materials offer high-voltage activity, they suffer from moisture-induced material instability during material storage/handling. Upon exposure to humidity, moisture-induced decomposition/phase transition can occur, which is detrimental to the electrochemical performance [26]. To gauge the stability, the effect of humidity on the structural stability of alluaudite type $Na_{2.27}Fe_{1.86}(SO_4)_3$ was probed by exposing the material in various RH (relative humidity) conditions using an X-ray diffractometer equipped with a sample chamber capable of controlling the relative humidity (RH-XRD). SDS-prepared alluaudite cathode was subjected to the humid environment inside the sample chamber using an RH generator at room temperature. The evolution of the XRD patterns was recorded at different RH (10–90%) with 1 h of rest time during consecutive measurements. Upon varying the humidity percentage, a rapid disappearance of the Bragg peaks pertaining to the alluaudite phase was noticed with increasing humidity till 70% RH (Fig. 5a). Subsequently, a mixture of alluaudite and bloedite $Na_2Fe(SO_4)_2{\cdot}4H_2O$ was obtained at 75% RH. Above 85% RH, alluaudite $Na_{2.27}Fe_{1.86}(SO_4)_3$ phase was completely transformed to the bloedite $Na_2Fe(SO_4)_2{\cdot}4H_2O$ phase as illustrated in Fig. 5b. Unlike other sulfate-based insertion materials (e.g., fluorosulfates $LiFeSO_4F$) leading to the formation of respective hydrated precursors ($FeSO_4{\cdot}nH_2O$, with $n = 1/4/7$) upon moisture attack, a clear alluaudite to bloedite phase transition was noticed. It is interesting to note that this is exactly the reverse reaction of bloedite to alluaudite phase transition observed during the material synthesis (Fig. 1). Overall, alluaudite sulfate was found to be prone to moisture attack leading to the formation of hydrated derivatives. Thus, these cathode systems warrant careful storage inside an inert atmosphere.

The ease and reversibility of alluaudite ↔ bloedite phase transition (Fig. 5c) inspired us to gauge the relative thermodynamic stability of these phases using (thermochemistry) calorimetric analysis. The solution calorimetric data

Table 3 Thermochemical cycles for enthalpy of formation for alluaudite $Na_2Fe_2(SO_4)_3$ and bloedite $Na_2Fe(SO_4)_2{\cdot}4H_2O$

Alluaudite $Na_2Fe_2(SO_4)_3$	***Enthalpy measurement***
$Na_2Fe_2(SO_4)_{3\ (s,\ 25\ °C)} + 6HCl_{\ (l,\ 25\ °C)} \rightarrow 2NaCl_{\ (sln,\ 25\ °C)} + 2FeCl_{2\ (sln,\ 25\ °C)} + 3H_2SO_{4\ (sln,\ 25\ °C)}$	$\Delta H_1 = \Delta H_{ds}\ [Na_2Fe_2(SO_4)_3]$
$Na_2SO_{4\ (s,\ 25\ °C)} + 2HCl_{\ (l,\ 25\ °C)} \rightarrow 2NaCl_{\ (sln,\ 25\ °C)} + H_2SO_{4\ (sln,\ 25\ °C)}$	$\Delta H_2 = \Delta H_{ds}\ (Na_2SO_4)$
$FeSO_{4\ (s,\ 25\ °C)} + 2HCl_{\ (l,\ 25\ °C)} \rightarrow FeCl_{2\ (sln,\ 25\ °C)} + H_2SO_{4\ (sln,\ 25\ °C)}$	$\Delta H_3 = \Delta H_{ds}\ (FeSO_4)$
$Na_2SO_{4\ (s,\ 25\ °C)} + FeSO_{4\ (s,\ 25\ °C)} \rightarrow Na_2Fe_2(SO_4)_{3\ (s,\ 25\ °C)}$	$\Delta H_4 = \Delta H°_f\ [Na_2Fe_2(SO_4)_3] = \mathbf{-\Delta H_1 + \Delta H_2 + 2\Delta H_3}$
Bloedite $Na_2Fe(SO_4)_2{\cdot}4H_2O$	***Enthalpy measurement***
$Na_2Fe(SO_4)_2{\cdot}4H_2O_{\ (s,\ 25\ °C)} + 4HCl_{\ (l,\ 25\ °C)} \rightarrow 2NaCl_{\ (sln,\ 25\ °C)} + FeCl_{2\ (sln,\ 25\ °C)} + 4H_2O_{\ (sln,\ 25\ °C)} + 2H_2SO_{4\ (sln,\ 25\ °C)}$	$\Delta H_5 = \Delta H_{ds}\ [Na_2Fe(SO_4)_2{\cdot}4H_2O]$
$Na_2SO_{4\ (s,\ 25\ °C)} + 2HCl_{\ (l,\ 25\ °C)} \rightarrow 2NaCl_{\ (sln,\ 25\ °C)} + H_2SO_{4\ (sln,\ 25\ °C)}$	$\Delta H_2 = \Delta H_{ds}\ (Na_2SO_4)$
$FeSO_{4\ (s,\ 25\ °C)} + 2HCl_{\ (l,\ 25\ °C)} \rightarrow FeCl_{2\ (sln,\ 25\ °C)} + H_2SO_{4\ (sln,\ 25\ °C)}$	$\Delta H_3 = \Delta H_{ds}\ (FeSO_4)$
$H_2O_{\ (l,25\ °C)} \rightarrow H_2O_{\ (sln,\ 25\ °C)}$	$\Delta H_6 = \Delta H_{ds}\ (H_2O)$
$Na_2SO_{4\ (s,\ 25\ °C)} + FeSO_{4\ (s,\ 25\ °C)} + 4H_2O_{\ (l,25\ °C)} \rightarrow Na_2Fe(SO_4)_2{\cdot}4H_2O_{\ (s,\ 25\ °C)}$	$\Delta H_7 = \Delta H°_f\ [Na_2Cu(SO_4)_2{\cdot}4H_2O] = \mathbf{-\Delta H_5 + \Delta H_2 + \Delta H_3 + 4\Delta H_6}$

Table 4 Thermochemical cycles for enthalpy of reaction (ΔH°_{rxn}) of alluaudite and water to form bloedite and iron sulfate

Reactions	Enthalpies (kJ/mol)
$Fe_{(s,\ 25\ ^{\circ}C)} + S_{(s,\ 25\ ^{\circ}C)} + 2O_{2\ (g\ 25\ ^{\circ}C)} \rightarrow FeSO_{4\ (s,\ 25\ ^{\circ}C)}$	$\Delta H_8 = -928.4$[a]
$2Na_{(s,\ 25\ ^{\circ}C)} + S_{(s,\ 25\ ^{\circ}C)} + 2O_{2\ (g,\ 25\ ^{\circ}C)} \rightarrow Na_2SO_{4\ (s,\ 25\ ^{\circ}C)}$	$\Delta H_9 = -1387.8 \pm 0.4$[b]
$H_{2\ (g,\ 25\ ^{\circ}C)} + 0.5O_{2\ (g,\ 25\ ^{\circ}C)} \rightarrow H_2O_{\ (l,\ 25\ ^{\circ}C)}$	$\Delta H_{10} = -285.83 \pm 0.1$[b]
$Fe_{(s,\ 25\ ^{\circ}C)} + 2Na_{(s,\ 25\ ^{\circ}C)} + 2SO_{4\ (s,\ 25\ ^{\circ}C)} + 4H_{2\ (g,\ 25\ ^{\circ}C)} + 2O_{2\ (g,\ 25\ ^{\circ}C)} \rightarrow Na_2Fe(SO_4)_2{\cdot}4H_2O$	$\Delta H_{11} = \Delta H_8 + \Delta H_9 + 4\Delta H_8 + \Delta H_7 = -3576.68 \pm 1.17$
$2Fe_{(s,\ 25\ ^{\circ}C)} + 2Na_{(s,\ 25\ ^{\circ}C)} + 3SO_{4\ (s,\ 25\ ^{\circ}C)} \rightarrow Na_2Fe_2(SO_4)_3$	$\Delta H_{12} = 2\Delta H_8 + \Delta H_9 + \Delta H_4 = -3256.36 \pm 1.31$
$Na_2Fe_2(SO_4)_{3(s,\ 25\ ^{\circ}C)} + 4H_2O_{\ (l,\ 25\ ^{\circ}C)} \rightarrow Na_2Fe(SO_4)_2{\cdot}4H_2O_{\ (s,\ 25\ ^{\circ}C)} + FeSO_{4\ (s,\ 25\ ^{\circ}C)}$	$\Delta H^{\circ}_{rxn} = \Delta H_{13} = \Delta H_{11} + \Delta H_8 - \Delta H_{12} - 4\ \Delta H_{10} = -105.52 \pm 1.80$

[a]NBS Tables [29]

[b]US Geological Survey [30]

are shown in Table 2. The corresponding thermochemical cycles used to calculate heats of formation are shown in Table 3. While the alluaudite has a Na-rich and Fe-deficient nature, bloedite is always stoichiometric. Reactions must be mass balanced for calculating the formation enthalpy. Thus, we assume the composition of alluaudite to be stoichiometric, i.e., $Na_2Fe_2(SO_4)_3$, in the thermochemical cycles and dissolution enthalpy calculations. Any small deviations from stoichiometry are not known reliably and would not affect the calorimetric data significantly. The enthalpy of solution (ΔH_{ds}) for bloedite was calculated by subtracting the contribution from $\Delta H_{ds}(FeSO_4)$, and the contributions from the minor secondary phases such as 1.92% $FeSO_4$ and 1.01% $Na_6Fe(SO_4)_4$ in the alluaudite were neglected since their contribution to ΔH_{ds} is < 2 kJ/mol.

The enthalpies of solution (ΔH_{ds}) in 5 N HCl at 25 °C are −38.47 ± 0.84 kJ/mol for alluaudite and 100.21 ± 0.94 kJ/mol for bloedite. The enthalpies of formation (ΔH°_f) of alluaudite and bloedite from their constituent binary sulfates, Na_2SO_4, and $FeSO_4$ (plus H_2O) were calculated using the thermochemical cycle in Table 3 and are exothermic. ΔH°_f of bloedite is −117.16 ± 1.10 kJ/mol and that of alluaudite is −11.76 ± 1.25 kJ/mol, indicating that the hydrated $Na_2Fe(SO_4)_2$ (bloedite) is significantly more energetically stable than the dehydrated $Na_2Fe_2(SO_4)_3$ (alluaudite). The calorimetric data support the observed synthesis and transformation (hydration-dehydration) pathways.

The endothermic DSC signals at 75–200 °C are due to dehydration of bloedite, and the endothermic peak at 290 °C confirms the formation of the alluaudite phase. The weight change in the sample before and after the DSC measurements corresponds to the loss of 4 mol of H_2O. The enthalpy of reaction (ΔH°_{rxn}) of alluaudite and water to form bloedite and $FeSO_4$ is calculated using the thermochemical cycle to be −105.52 ± 1.80 kJ/mol (Table 4). This exothermic reaction is the driving force for the formation of bloedite which

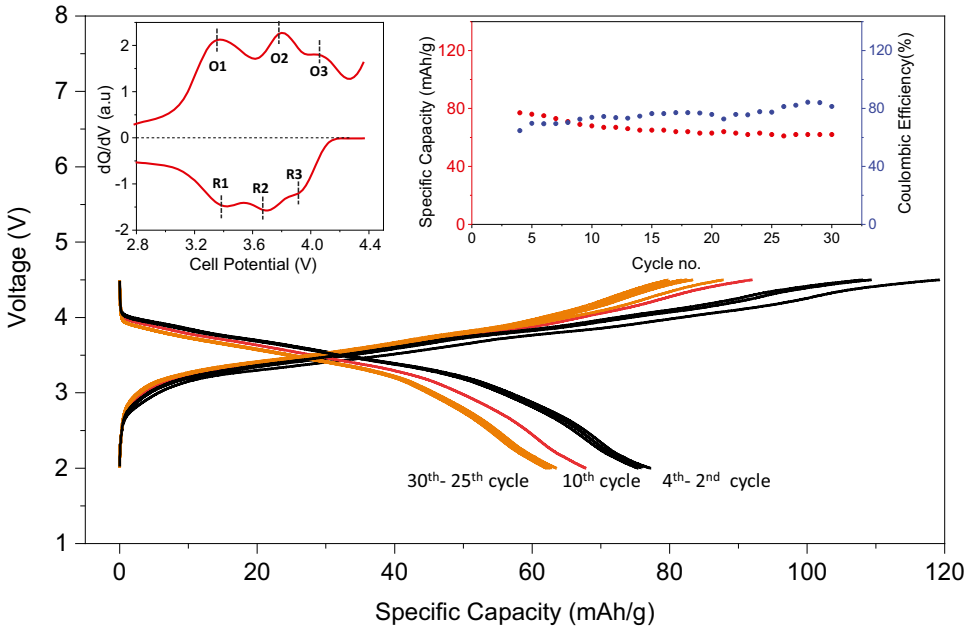

Fig. 6 Galvanostatic charge–discharge profiles of $Na_{2.27}Fe_{1.86}(SO_4)_3$ synthesized by spray drying method at a rate of C/20 (2Na in 20 h) at 25 °C. (Inset, left) Corresponding *dQ*/*dV* plot showing three distinct broad redox peaks with average potential located at 3.7–3.8 V (vs. Na/Na^+). (Inset, right) Cycling stability and Coulombic efficiency for the first 30 cycles

is the more stable phase. Thus, the thermochemical data confirm sulfates readily react with water to form their hydrated derivative products. This thermodynamically driven water reactivity may present a problem in their application in batteries making inert storage essential.

Finally, the electrochemical activity of spray drying prepared alluaudite $Na_{2.27}Fe_{1.86}(SO_4)_3$ was checked as a cathode material in a Na-ion half-cell architecture without any particle size optimization or additional carbon nano-painting. The room-temperature galvanostatic charge–discharge profile showed a reversible sodium (de)insertion with a reversible discharge capacity of ~77 mAh/g (Fig. 6) at a rate of C/20, which is ~80% of the theoretical capacity ($Q_{TH} = 100$ mAh/g). After 30 cycles, the specific capacity decreased to 62 mAh/g. From the dQ/dV curve (Fig. 6, inset), three sets of broad redox peaks were clearly visible at around 3.3 V, 3.7 V, and 4.0 V, leading to the nominal redox potential ~3.8 V (vs. Na/Na^+). Without any cathode optimization, this desirable electrochemical activity could be attributed to the inherent open framework of alluaudites. Further, the addition of ascorbic acid as a carbon source and complexing agent and the nanometric-rich spherical morphology rendered the initial microstructural advantage to the cathodic performance. With further cathode optimization and suitable choice of electrolytes (and additives), the electrochemical activity of spray drying prepared alluaudite can be further improved.

Conclusions

In summary, this work demonstrates the aqueous-based two-step spray drying synthesis of alluaudite $Na_{2+2x}Fe_{2-x}(SO_4)_3$ sodium insertion material. The presence of liquid media assures atomic-level mixing and easy ionic diffusion, facilitating alluaudite formation with shorter annealing. Solution calorimetry confirmed that hydrated $Na_2Fe(SO_4)_2$ (i.e., bloedite) is substantially more energetically stable than the dehydrated phase assemblage containing alluaudite $Na_2Fe_2(SO_4)_3$. Thus, hydration is strongly thermodynamically driven and may be a limitation in using alluaudite for battery applications. The calorimetric data support the observed synthesis and transformation (hydration-dehydration) pathways. It is once again proved that sulfate-based materials need to be handled carefully to prevent moisture attack by providing a detailed analysis on how the alluaudite phase completely changes to the bloedite phase on raiding relative humidity. The spray drying–made alluaudite material was found to deliver reversible high-voltage (ca. 3.8 V) operation without any material optimization. Spray drying route can be extended to the scalable economic preparation of various sulfate classes of polyanionic battery insertion materials.

Supplementary information The online version contains supplementary material available at https://doi.org/10.1007/s10008-022-05142-w.

Funding Open Access funding enabled and organized by Projekt DEAL. The Science and Engineering Research Broad (SERB, Govt. of India) provided financial support under the Early Career Research Award (ECR/2015/000525). The first author (PB) received from the Department of Science and Technology (DST) an INSPIRE fellowship (IF180127). DD received from the International Centre for Diffraction Data (ICDD, USA) a Ludo Frevel crystallography fellowship and from the Electrochemical Society (ECS, USA) an H.H. Uhlig Summer Fellowship. A.N. and K.J. received financial support from the U.S. Department of Energy, Office of Basic Energy Sciences, Grant DE-FG02-03ER46053.

Declarations

Competing interests The authors declare no competing interests.

References

1. Yabuuchi N, Kubota K, Dahbi M, Komaba S (2014) Research development on sodium-ion batteries. Chem Rev 114:11636–11682
2. Manthiram A, Goodenough JB (1989) Lithium insertion into $Fe_2(SO_4)_3$ frameworks. J Power Sources 26:403–408
3. Barpanda P (2016) Pursuit of sustainable iron-based sodium battery cathodes: two case studies. Chem Mater 28:1006–1011
4. Barpanda P, Lander L, Nishimura S, Yamada A (2018) Polyanionic insertion materials for sodium-ion batteries. Adv Energy Mater 8:1703055
5. Padhi AK, Nanjundaswamy KS, Goodenough JB (1997) Phospho-olivines as positive-electrode materials for rechargeable lithium batteries. J Electrochem Soc 144:1188–1194
6. Barpanda P, Oyama G, Nishimura S, Chung SC, Yamada A (2014) A 3.8-V earth-abundant sodium battery electrode. Nat Commun 5:4358
7. Fisher DJ (1955) Alluaudite. Am Min 40:1100–1109
8. Dwibedi D, Barpanda P, Yamada A (2020) Alluaudite battery cathodes. Small. Methods 4:2000051
9. Trad K, Carlier D, Croguennec L, Wattiaux A, Ben Amara M, Delmas C (2010) $NaMnFe_2(PO_4)_3$ alluaudite phase: synthesis, structure, and electrochemical properties as positive electrode in lithium and sodium batteries. Chem Mater 22:5554–5562
10. Dwibedi D, Araujo RB, Chakraborty S, Shanbogh PP, Sundaram NG, Ahuja R, Barpanda P (2015) $Na_{2.44}Mn_{1.79}(SO_4)_3$: a new member of the alluaudite family of insertion compounds for sodium ion batteries. J Mater Chem A 3:18564–18571
11. Dwibedi D, Gond R, Dayamani A, Araujo RB, Chakraborty S, Ahuja R, Barpanda P (2017) $Na_{2.32}Co_{1.84}(SO_4)_3$ as a new

member of the alluaudite family of high-voltage sodium battery cathodes. Dalton Trans 46:55–63
12. Ming J, Barpanda P, Nishimura S, Okubo M, Yamada A (2015) An alluaudite $Na_{2+2x}Fe_{2-X}(SO_4)_3$ (x=0.2) derivative phase as insertion host for lithium battery. Electrochem Commun 51:19–22
13. Oyama G, Nishimura S, Suzuki Y, Okubo M, Yamada A (2015) Off-stoichiometry in alluaudite-type sodium iron sulfate $Na_{2+2x}Fe_{2-X}(SO_4)_3$ as an advanced sodium battery cathode material. ChemElectroChem 2:1019–1023
14. Dwibedi D, Ling CD, Araujo RB, Chakraborty S, Duraisamy S, Munichandraiah N, Ahuja R, Barpanda P (2016) Ionothermal synthesis of high-voltage alluaudite $Na_{2+2x}Fe_{2-X}(SO_4)_3$ sodium insertion compound: Structural, electronic, and magnetic insights. ACS Appl Mater Interfaces 8:6982–6991
15. Dwibedi D, Baskar S, Barpanda P (2017) Sustainable aqueous synthesis and electrochemical insights on high-voltage sodium alluaudite insertion materials. ECS Trans 80:337–342
16. Rahaman MN (2017) Ceramic Processing and Sintering. CRC Press
17. Rietveld H (1969) A profile refinement method for nuclear and magnetic structures. J Appl Crystallogr 2:65–71
18. Larson A, Von Dreele R (2000) Report Laur 86–748. Los Alamos National Laboratory, New Mexico, USA
19. Toby B (2001) Expgui, a graphical user interface for Gsas. J Appl Crystallogr 34:210–213
20. Momma K, Izumi F (2008) Vesta: a three-dimensional visualization system for electronic and structural analysis. J Appl Crystallogr 41:653–658
21. Kilday MV (1980) The enthalpy of solution of srm 1655 (KCl) in H_2O. J Res Natl Bur Stand (US) 85:467
22. Zones SI, Jayanthi K, Pascual J, Xie D, Navrotsky A (2021) Energetics of the local environment of structure-directing agents influence zeolite synthesis. Chem Mater 33:2126–2138
23. Meng Y, Yu T, Zhang S, Deng C (2016) Top-down synthesis of muscle-inspired alluaudite $Na_{2+2x}Fe_{2-X}(SO_4)_3$/SWNT spindle as a high-rate and high-potential cathode for sodium-ion batteries. J Mater Chem A 4:1624–1631
24. Mineralogical database (2000) http://www.mindat.org
25. Singh S, Jha PK, Avdeev M, Zhang W, Jayanthi K, Navrotsky A, Alshareef HN, Barpanda P (2021) Marinite $Li_2Ni(SO_4)_2$ as a new member of the bisulfate family of high-voltage lithium battery cathodes. Chem Mater 33:6108–6119
26. Zhang L, Tarascon JM, Sougrati MT, Rousse G, Chen G (2015) Influence of relative humidity on the structure and electrochemical performance of sustainable $LiFeSO_4F$ electrodes for Li-ion batteries. J Mater Chem A 3:16988–16997
27. Radha A, Lander L, Rousse G, Tarascon JM, Navrotsky A (2015) Thermodynamic stability and correlation with synthesis conditions, structure and phase transformations in orthorhombic and monoclinic Li2M(SO4)2 (M= Mn, Fe Co, Ni) polymorphs. J Mater Chem A 3:2601–2608
28. Parker VB (1965) National standard reference data series, National Bureau of Standards. 2:66
29. Wagman DD, Evans WH, Parker VB, Schumm RH, Halow I, Bailey SM, Churney KL, Nuttall RL (1982) The NBS tables of chemical thermodynamic properties. J Phys Chem Ref Data Suppl 2 National Bureau of Standards, Washington DC 20234, 177. 11:1807–1812
30. Robie R, Hemingway B (1995) Thermodynamic properties of minerals and related substances at 298.15 K and 1 bar (105 Pascals) and at higher temperatures. Bull US Geol Surv 2131:461